

# Electronic Structure, Oxidation State of Sn, and Chemical Stability of Photovoltaic Perovskite Variant $\text{Cs}_2\text{SnI}_6$

Zewen Xiao,<sup>1,2</sup> Hechang Lei,<sup>2,3</sup> Xiao Zhang,<sup>2</sup> Yuanyuan Zhou,<sup>4</sup> Hideo Hosono,<sup>1,2</sup> and Toshio Kamiya<sup>\*,1,2</sup>

<sup>1</sup>Materials and Structures Laboratory, Tokyo Institute of Technology, Yokohama 226-8503, Japan

<sup>2</sup>Materials Research Center for Element Strategy, Tokyo Institute of Technology, Yokohama 226-8503, Japan

<sup>3</sup>Department of Physics, Renmin University of China, Beijing 100872, China

<sup>4</sup>School of Engineering, Brown University, Providence, Rhode Island 02912, United States

\*Email: kamiya.t.aa@m.titech.ac.jp

**ABSTRACT:**  $\text{Cs}_2\text{SnI}_6$ , a variant of perovskite  $\text{CsSnI}_3$ , is expected for a photovoltaic material. Based on a simple ionic model, it is expected that  $\text{Cs}_2\text{SnI}_6$  is composed of  $\text{Cs}^+$ ,  $\text{I}^-$ , and  $\text{Sn}^{4+}$  ions and that the band gap is primarily made of occupied  $\text{I}^-$   $5\text{p}^6$  valence band maximum (VBM) and unoccupied  $\text{Sn}^{4+}$   $5\text{s}$  conduction band minimum (CBM) similar to  $\text{SnO}_2$ . In this work, we performed density functional theory (DFT) calculations and revealed that the real charge state of the Sn ion in this compound is +2 similar to  $\text{CsSnI}_3$ . This is due to strong covalent nature between the I ion and the Sn ion, the VBM consists of  $\text{I}$   $5\text{p}$  –  $\text{I}$   $5\text{p}$  antibonding states, and the CBM of  $\text{I}$   $5\text{p}$  –  $\text{Sn}$   $5\text{s}$  antibonding states. The +2 oxidation state of Sn is realized by the apparent charge state of  $\text{I}^{-2/3}$ , because the  $\text{I}$   $5\text{p}$  –  $\text{Sn}$   $5\text{s}$  antibonding states form the unoccupied CBM and apparently 1/18 of the  $\text{I}$   $5\text{p}$  orbitals are unoccupied. These results are further supported by comparing chemical bonding analyses with those of related compounds. The chemical stability of the  $\text{Cs}_2\text{SnI}_6$  phase is explained by the strong covalent bonds between Sn and I.

**KEYWORDS:** Tin halide, Perovskite, Electronic structure, Oxidation state, Bonding, DFT

## 1. INTRODUCTION

Lead halide perovskites invoked new development research in the third-generation photovoltaics because of the high power conversion efficiencies (PCE) of those photovoltaic cells as high as 20.1%.<sup>1–6</sup> These compounds are represented by the general chemical formula  $ABX_3$  ( $A = \text{Cs}$ ,  $\text{CH}_3\text{NH}_3$ , or  $\text{CH}_2\text{NH}=\text{CH}$ ;  $B = \text{Pb}$  or  $\text{Sn}$ ;  $X = \text{I}$ ,  $\text{Br}$  or  $\text{Cl}$ ), where the  $A$  cations are located in the cubic network of corner-sharing  $\text{BX}_6$  octahedra. However, these compounds and their devices suffer from the long-term instability in an ambient atmosphere, and the water-soluble toxic lead components are potential risk for the environment issue. Therefore, Sn derivatives of provskite compounds,  $\text{ASnX}_3$ , have been examined.<sup>7–9</sup> However, these  $\text{ASnX}_3$  perovskites are very sensitive to the ambient atmosphere (oxygen, moisture, etc.).<sup>7–11</sup> The instability of  $\text{ASnX}_3$  is suggested to be related to unintentional oxidation of  $\text{Sn}^{2+}$  to  $\text{Sn}^{4+}$ , which might lead to a structural transformation and then degrade the photovoltaic performance.<sup>8,9</sup> Therefore, one may expect that the Sn-based perovskite compounds would be stabilized if a +4 oxidation state of  $\text{Sn}^{4+}$  is employed. With this line, a class of perovskite variants  $\text{A}_2\text{SnX}_6$  would be attractive candidates<sup>12</sup> because Sn in  $\text{A}_2\text{SnX}_6$  is expected to be the +4 oxidation state upon assumption of the  $\text{A}^+$  and  $\text{X}^-$  ion states, which would lead to the expectation that the conduction band minimum (CBM) is formed by Sn 5s, similar to the case of  $\text{SnO}_2$ .<sup>13</sup>  $\text{Cs}_2\text{SnI}_6$ , as a typical example, has been reported to be air-stable and  $\text{Cs}_2\text{SnI}_6$  based solar cells have exhibited promising PCEs up to 7.8% due to its intrinsic stability and beneficial optoelectronic properties.<sup>14</sup> However, it is not clear whether such simple ionic model is applied to complex materials in which both ionic and covalent natures coexist.

Density functional theory (DFT) calculations have widely been employed to understand electronic structures and chemical bonding nature.<sup>15–17</sup> On the other hand, there is ambiguity to estimate the oxidation states of ions because there is not a unique accepted method to attribute charges distributing in the inter-ion spaces to each ion. Therefore, many charge analysis methods have been proposed and employed, which include Mulliken population analysis,<sup>18</sup> natural bond analysis, Barder analysis,<sup>19</sup> and Born effective charges.<sup>20</sup> Among them, Mulliken population analysis is fit to atomic orbital basis but not easily applied to plane wave (PW) basis sets. Further, there is ambiguity how to divide the non-diagonal term of the density matrix to bonding ions. Some PW method codes like Vienna Ab initio Simulation Program (VASP) counts electron density within a given sphere with a radius  $R_{\text{ws}}$  to estimate the total electron number  $n_{\text{e}}(R_{\text{ws}})$  for

each atom; however, the result depends on the choice of  $R_{ws}$ , and usually underestimate  $R_{ws}$ . Bader analysis divide all the space in unit cell to ions based on the Bader partitioning scheme; therefore, it would be reasonable to expect the underestimation issue by the above method would be improved. Born effective charges appear to provide good values for materials with small dielectric permittivity, but gives extraordinary large values with high anisotropy for materials with large dielectric permittivity.

In this work, we investigated the electronic structure and oxidation states of  $\text{Cs}_2\text{SnI}_6$  by DFT calculations. We found that while the valence band maximum (VBM) consists of I 5p – I 5p antibonding states as expected, the CBM, unexpectedly, consists of I 5p – Sn 5s antibonding states. The Sn 5s orbitals indeed form electronic states  $\sim 7$  eV deeper than the VBM and are fully occupied, indicating that Sn in  $\text{Cs}_2\text{SnI}_6$  should be in the +2 oxidation state. To discuss the valences states of the constituent ions, we examined different methods and finally chose Bader analysis. The calculated oxidation state of I is a bit smaller than -1 and to be -2/3, because apparently 1/18 of the I 5p orbitals are unoccupied due to the I 4p – Cs 6s antibonding CBM state. We will discuss the origin of the chemical stability of the  $\text{Cs}_2\text{SnI}_6$  phase based on these results.

## 2. COMPUTATIONAL METHOD

DFT calculations were performed using the projector-augmented plane wave (PAW) method implemented in the VASP 5.3.<sup>21</sup> Cs (5s)(5p)(6s), Sn (5s)(5p), and I (5s)(5p) are treated as oxidation states in the PAW potentials. The plane wave cutoff energy was set to 275.4 eV. For the exchange-correlation functional, we confirmed that the local density approximation (LDA) and the Perdew–Burke–Ernzerhof (PBE96)<sup>22</sup> generalized gradient approximation (GGA) functionals underestimated the band gap for  $\text{Cs}_2\text{SnI}_6$  (0.41 and 0.25 eV, respectively as listed in Table 1. The experimental value is 1.26 eV<sup>14</sup>). On the other hand, the Heyd–Scuseria–Ernzerhot (HSE06)<sup>23</sup> hybrid functional, which incorporates  $\alpha = 25$  % of Hartree-Fock exact exchange contribution and  $1-\alpha = 75$  % of PBE96 contribution, provided a better band gap value of 0.93 eV but still smaller than the experimental value. In order to discuss the chemical bonding nature and the origin of the band gap more realistically, we adjusted the  $\alpha$  to be 34 % so as to reproduce the reported band gap value, and the HSE06 with this  $\alpha$  value will be used for the following discussion. A primitive cell containing one formula unit (f.u.) of  $\text{Cs}_2\text{SnI}_6$  and a  $\Gamma$ -centered  $4 \times 4$

$\times 4$   $k$ -mesh were employed for the periodic calculations. Prior to the electronic structure calculations, variable-cell structure relaxations were performed. Electron localization function (ELF)<sup>24</sup> was calculated by VASP for chemical bonding analysis. The two-dimensional (2D) contour maps of ELF were displayed by the VESTA program.<sup>25</sup> To reveal the origin of the band gap in  $\text{Cs}_2\text{SnI}_6$ , we also performed calculations for several hypothetic structures including  $\text{I}_6^0$  cluster,  $[\text{SnI}_6]^{2-}$  cluster, and  $[\text{SnI}_6]^{2-}$  sublattice models. Additionally, chemical bonding analysis was carried out for  $\text{Cs}_2\text{SnI}_6$  based on the crystal orbital Hamiltonian population (COHP)<sup>26</sup> calculated by a tight binding–linear muffin tin orbitals–atomic sphere approximation (TB-LMTO-ASA) program,<sup>27</sup> where positive –COHP values indicate bonding states and vice versa. Integration of the –COHP spectrum up to the Fermi level ( $E_F$ ) yielded –ICOHP values as measure of total overlap populations (in other words, the bond order). The Bader charge analysis was carried out by the Bader program<sup>28</sup> with the charge density obtained by VASP.

### 3. RESULTS AND DISCUSSION

**3.1. Electronic Structure.**  $\text{Cs}_2\text{SnI}_6$  crystalizes into the face-centered-cubic (fcc)  $\text{K}_2\text{PtCl}_6$ -type with the space group  $Fm\text{-}3m$  (the anti-fluorite structure) and the lattice parameter  $a$  of  $11.65\text{ \AA}$ .<sup>29</sup> As shown in Figure 1a, the unit cell is composed of four  $[\text{SnI}_6]^{2-}$  octahedra at the corners and the face centers and eight  $\text{Cs}^{2+}$  cations at the tetragonal interstitials. Alternatively,  $\text{Cs}_2\text{SnI}_6$  can be regarded as a defective variant of the perovskite  $\text{CsSnI}_3$ , in which the  $[\text{SnI}_6]$  octahedra connect to each other by sharing their corners. The  $\text{Cs}_2\text{SnI}_6$  structure is obtained by removing a half of the Sn atoms in the  $\text{CsSnI}_3$  structure at intervals (i.e. the edge centers and the body center in Figure 1a), and thus the corner-shared  $[\text{SnI}_6]^{2-}$  octahedra become isolated in  $\text{Cs}_2\text{SnI}_6$ . After the half of the Sn atoms are removed, the  $[\text{SnI}_6]^{2-}$  octahedra shrink slightly, leading to the smaller Sn–I bond length ( $2.85\text{ \AA}$ )<sup>29</sup> in  $\text{Cs}_2\text{SnI}_6$  than that in  $\text{CsSnI}_3$  ( $3.11\text{ \AA}$ )<sup>10</sup> as well as the smaller intraoctahedral I–I bond length ( $4.04\text{ \AA}$ ) than that of interoctahedral I–I' bond lengths ( $4.20\text{ \AA}$ ) (Figure 1b). Table 1 summarizes the literature and calculated lattice parameters, bonding lengths, and band gaps. Compared with the LDA and PBE96, the HSE06 gave better results, as it often does for semiconductors.<sup>30</sup> In particular, when  $\alpha = 34\%$ , the HSE06 provided the lattice parameters and bonding lengths within 1.5% errors from the room-temperature experimental values and reproduced the experiment band gap value.

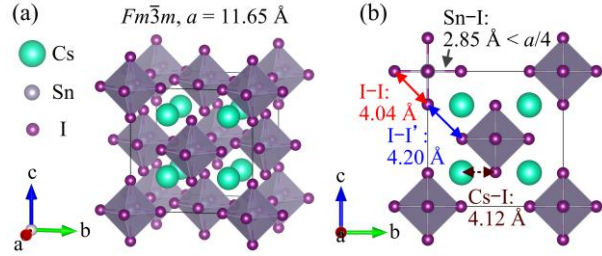


**Figure 1.** (a) Crystal structure of  $\text{Cs}_2\text{SnI}_6$  and (b) top view of (a). The bonding lengths from Ref. 28 are shown in (b).

**Table 1. Literature and calculated lattice parameters, bonding lengths, and band gaps ( $E_g$ ) of  $\text{Cs}_2\text{SnI}_6$ .**

	Exp.	LDA	PBE96	HSE06 ( $\alpha=25\%$ )	HSE06 ( $\alpha=34\%$ )
$a$ (Å)	11.65 <sup>29</sup>	11.92	12.03	11.86	11.82
$\text{Cs}-\text{I}$ (Å)	4.12 <sup>29</sup>	4.22	4.25	4.19	4.18
$\text{Sn}-\text{I}$ (Å)	2.85 <sup>29</sup>	2.83	2.91	2.89	2.88
$\text{I}-\text{I}$ (Å)	4.04 <sup>29</sup>	4.00	4.11	4.09	4.07
$\text{I}-\text{I}'$ (Å)	4.20 <sup>29</sup>	4.43	4.39	4.30	4.29
$E_g$ (eV)	1.26 <sup>14</sup>	0.41	0.25	0.93	1.26

**3.2. Electronic Structure.** Figures 2a and b show the calculated band structure and the total and projected densities of states (DOSs) for  $\text{Cs}_2\text{SnI}_6$  with the HSE06, respectively. The band structure of  $\text{Cs}_2\text{SnI}_6$  exhibits a direct band gap of 1.26 eV at the  $\Gamma$  point, which is close to the experimental value.<sup>14</sup> The valence band (VB) consists of I 5p orbitals, and its band width is small (only 2.38 eV in the total width). Below the VB, there is another I 5p band localized between -2.90 and -3.62 eV, which is slightly hybridized with Sn 5p orbitals. The Sn 5s orbital forms a very deep band between -7.18 and -6.84 eV, and has little contribution to the VB. On the other hand, the conduction band (CB) extends from 1.26 to 2.56 eV and mainly consists of I 5p orbitals hybridized with Sn 5s orbitals. This breaks the above expectation in Introduction that the CBM could consist of Sn 5s orbitals based on the simple ionic model of  $\text{Cs}^+{}_2\text{Sn}^{4+}\text{I}^-{}_6$ . Upper CB bands starts from 4.86 eV and separate from the CB with a forbidden gap of 2.30 eV, which

consist of Sn 5p, Cs 6s, 5d and I 6s, 5d orbitals. It can also be seen that the Cs ion has little contribution to the VB and the CB.

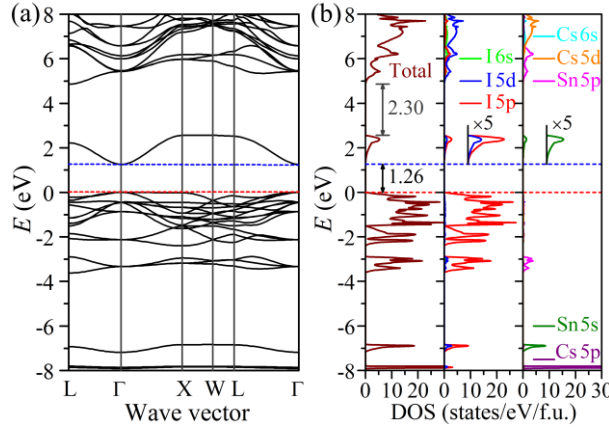


**Figure 2.** (a) Band structure and (b) total and projected DOSs of  $\text{Cs}_2\text{SnI}_6$  calculated with HSE06. The red and blue dashed lines mark the VBM and the CBM, respectively.

**3.3. Chemical Bonding Analysis.** We then analyze the character and strength of chemical bonds by COHP as shown in Figure 3a along with the total DOS. It can be seen that the Sn–I bonds are all bonding states below  $E_F$  while antibonding ones above  $E_F$ . It should be noted that there are strong bonding states at  $\sim -7.4$  and  $-3.2$  eV, which originate from the strong covalent interaction between Sn 5s/5p and I 5p states. The strong covalent interaction also leads to the largest  $-\text{ICOHP}$  (2.41 eV/bond) for the Sn–I bond. In contrast, the small  $-\text{ICOHP}$  value (0.10 eV/bond) for the Cs–I bond reflects the weak covalent interaction between Cs and I. On the other hand, the  $-\text{COHP}$  spectra of I–I and I–I' bonds show similar patterns between  $-2.2$  and  $0$  eV, where the DOS is contributed dominantly by the I 5p state. This pattern recalls the familiar molecular orbital (MO) diagrams of homonuclear molecular dimers and clusters. The large antibonding states at  $E_F$  and the negative small  $-\text{ICOHP}$  values ( $-0.24$  and  $-0.064$  eV/bond for the I–I and I–I' bonds, respectively) imply that the MOs of I 5p are almost filled up and no effective bond strength remains between the I ions. The bonding natures are confirmed also by the valence electron density maps on the (200) and (400) planes, as shown in Figure 3b and 3c, respectively. It can be seen that the significant electron distribution in the Sn–I bonds clearly indicate the formation of Sn–I covalent bond. In contrast, there is little electrons between Cs–I, meaning that little covalent bond exist in the Cs–I bonds.

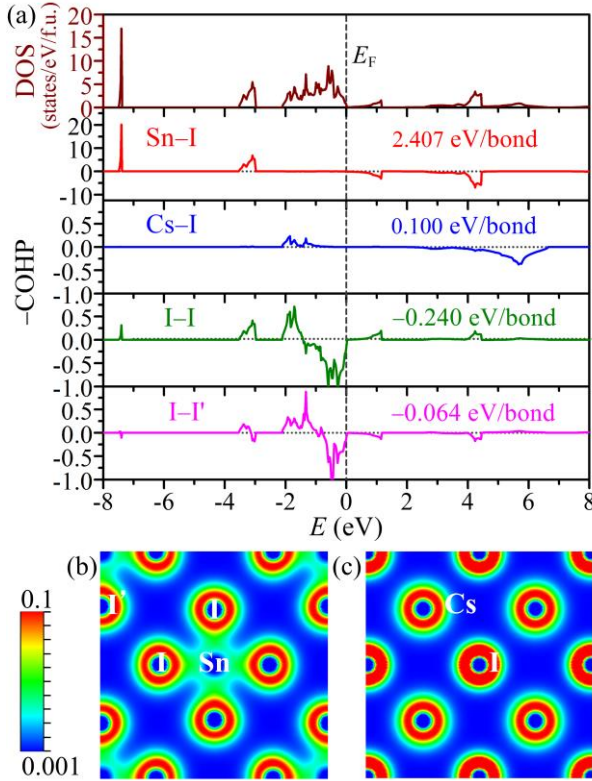


**Figure 3.** (a) Calculated –COHPs for Sn–I, Cs–I, I–I, and I–I' bonds. The total DOS is shown in the top panel for comparison. The –ICOHP values for Sn–I, Cs–I, I–I, and I–I' are also shown in respective panels. (b and c) Valence electron density maps on the (b) (200) and (c) (400) planes.

**3.4. Origin of Band Gap.** To understand the chemical bonding nature and the origin of the band gap in  $\text{Cs}_2\text{SnI}_6$ , we performed DFT calculations for some hypothetic structures. First we examined the electronic structure for an isolated  $\text{I}_6$  octahedron (i.e.,  $\text{I}_6^0$  cluster), as shown in Figure 4a. According to the energy eigenvalues at the  $\Gamma$  point (Table S1 in Supporting Information) and the group theory, the 18 I 5p orbitals of the  $\text{I}_6$  octahedra are split to 7 groups.<sup>31</sup> The 6 radial I 5p orbitals split to 3 groups of  $a_{1g}$  (I–I bonding) and  $e_g$  &  $t_{1u}$  (I–I antibonding). The 12 tangential I 5p orbitals form 4 triply degenerated groups of  $1t_{1u}$  &  $t_{2g}$  (I–I bonding) and  $t_{2u}$  &  $t_{1g}$  (I–I antibonding). These groups are qualitatively arranged on the energy scale in Figure 4d.

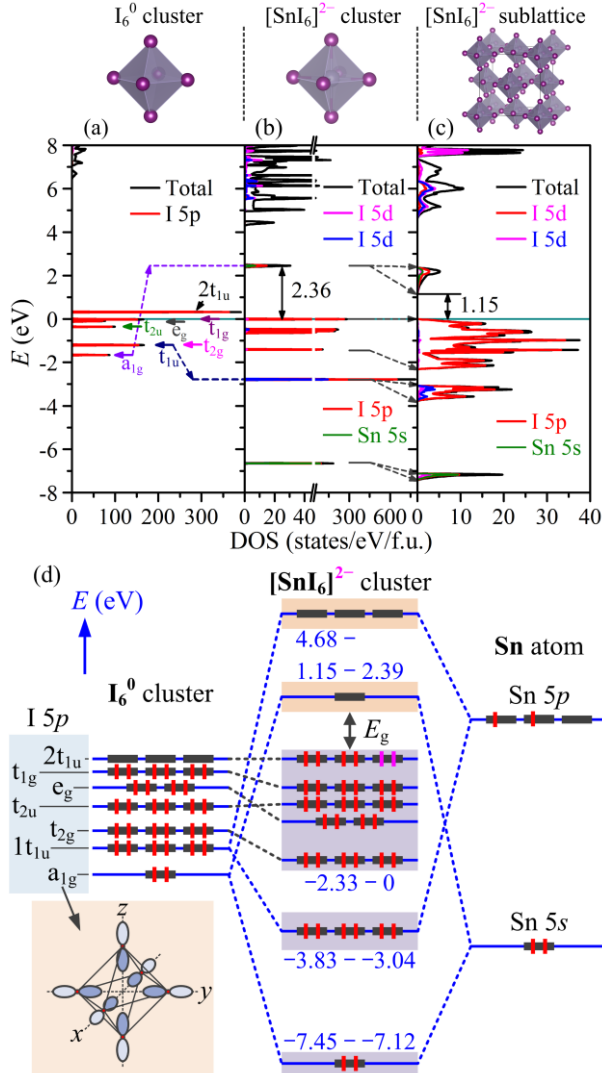


**Figure 4.** Total and projected DOSs of (a)  $I_6^0$  cluster, (b)  $[SnI_6]^{2-}$  cluster, and (c)  $[SnI_6]^{2-}$  sublattice models. The structures of the  $I_6$  cluster, the  $SnI_6$  cluster and the  $SnI_6$  sublattice models are shown on top. (d) Qualitative interaction diagram for the  $I_6^0$  cluster, the  $SnI_6$  cluster, and the  $SnI_6$  sublattice models. The orbitals are qualitatively arranged on the energy scale. Inset of (d) shows a schematic illustration of  $I_6$   $a_{1u}$  orbital.

By adding an Sn atom and 2 electrons (transferred from the two Cs atoms, which is ionized to  $Cs^+$  in  $Cs_2SnI_6$ ) into the  $I_6$  octahedron, we calculated the electronic structure of a  $[SnI_6]^{2-}$  octahedron cluster. The resulted DOSs are shown in Figure 4b and the derived energy levels (Table S1 in Supporting Information) are qualitatively illustrated in Figure 4d. The shallow Sn 5p orbitals slightly hybridize with the  $I_6$   $t_{1u}$  orbitals, leading to Sn 5p –  $I_6$   $t_{1u}$  bonding states at -2.77 eV and Sn 5p –  $I_6$   $t_{1u}$  antibonding states at 5.45 eV. The deep Sn 5s orbitals strongly

hybridize with the  $I_6$   $a_{1g}$  orbitals (see the inset to Figure 4d), resulting in the  $Sn\ 5s - I_6\ a_{1g}$  bonding states at  $-6.65$  eV and the  $Sn\ 5s - I_6\ a_{1g}$  antibonding states at  $2.36$  eV. These results are consistent with the  $-COHP$  analysis of  $Sn-I$  (the second panel of Figure 3a). The  $Sn\ 5s$  and  $5p$  orbitals have little hybridization with the other 5 groups of  $I\ 5p$  orbitals (i.e.  $t_{2g}$ ,  $t_{2u}$ ,  $e_g$ ,  $t_{1g}$  and  $2t_{1u}$ ). Note that the  $2t_{1u}$  orbitals are fully occupied while the  $Sn\ 5s - I_6\ a_{1g}$  antibonding orbital is unoccupied in the  $[SnI_6]^{2-}$  cluster, and the  $[SnI_6]^{2-}$  cluster forms a semiconductor-type electronic structure with the band gap of  $2.36$  eV.

Finally, we calculated a  $[SnI_6]^{2-}$  sublattice model in which  $[SnI_6]^{2-}$  are located at the corner and the face-center sites in the unit cell of  $Cs_2SnI_6$  (i.e., the  $Cs^+$  ions are removed from  $Cs_2SnI_6$ ). The resulted DOSs (Figure 4c) are very similar to that of  $Cs_2SnI_6$  (Figure 2b), indicating that  $Cs^+$  cations have limited contribution to the electronic structure of  $Cs_2SnI_6$  except for slightly pushing up the bands above  $E_F$ . The localized orbitals in the  $[SnI_6]^{2-}$  cluster model expand into dispersed bands made of the  $[SnI_6]^{2-}$  sublattice. The unoccupied  $Sn\ 5s - I_6\ a_{1g}$  antibonding orbitals forms the CBM, and the occupied  $I_6\ 5p$  ( $t_{2g}$ ,  $t_{2u}$ ,  $e_g$ ,  $t_{1g}$ , and  $2t_{1u}$ ) orbitals, which are antibonding between two  $I$  ions while non-bonding states to  $Sn$ , form the VBM.

**3.5. Oxidation state of Sn.** From the electronic structure discussed above, the  $Sn\ 5s$  orbitals are much deeper than the VB and fully occupied by electrons; therefore, the  $Sn$  ion in  $Cs_2SnI_6$  would be interpreted well by the  $+2$  oxidation state. The  $Sn^{2+}$  and  $Cs^+$  states suggest that the apparent oxidation state of  $I$  is  $-2/3$  ( $5p^{5/2/3}$ ), smaller than the conventional formal charge of  $-1$  ( $5p^6$ ); this is understood by the above electronic structure that some of  $I\ 5p$  orbitals are unoccupied states because the unoccupied CBM state is formed mainly by the  $I_6\ a_{1g} - Sn\ 5s$  antibonding state. The  $Sn^{2+}$  and  $I^{-2/3}$  states can also be perceived by the ionic distance analysis. Table 2 shows the literature bonding lengths and the ones estimated from the literature ionic radii.<sup>32,33</sup> The bonding lengths estimated from the ionic radii of  $Cs^+$  ( $1.88$  Å),  $Sn^{2+}$  ( $1.02$  Å), and  $I^-$  ( $2.20$  Å) explain well the actual ones in  $CsSnI_3$ ,<sup>10</sup> but not in  $Cs_2SnI_6$ ; *i.e.*, compared with the  $Sn-I$  length estimated using the  $Sn^{2+}$  radius ( $3.22$  Å), the one using the  $Sn^{4+}$  radius ( $2.89$  Å) is closer to the actual value ( $2.85$  Å), which seems inconsistent with the  $Sn^{2+}$  state in  $Cs_2SnI_6$ . This apparent inconsistency is caused by the improper assumption of the  $I^-$  state and its ionic radius, as the radius of  $I^-$  is larger than the actual  $I^{-2/3}$  anion in  $Cs_2SnI_6$ . The radius of  $I^{-2/3}$  ion is unknown, but it would reasonably be estimated to be  $2.02$  Å from the  $I-I$  length ( $4.04$  Å), which

improves the estimated  $\text{Sn}^{2+}$ –I length to 3.08 Å and makes it consistent with the +2 oxidation state of Sn.

**Table 2. Literature bonding lengths, the ideal ionic ones estimated from the literature ion radii of 1.88 (Cs<sup>+</sup>), 0.69 (Sn<sup>4+</sup>), 1.02 (Sn<sup>2+</sup>), and 2.20 Å (I<sup>−</sup>) and the covalent ones from the proposed radius of 2.02 Å for I<sup>−2/3</sup> anion for CsSnI<sub>3</sub> and Cs<sub>2</sub>SnI<sub>6</sub>.**

	CsSnI <sub>3</sub> <sup>10</sup>	Ionic (I <sup>−</sup> )	Cs <sub>2</sub> SnI <sub>6</sub> <sup>29</sup>	Covalent (I <sup>−2/3</sup> )
Cs–I (Å)	4.39	4.22	4.12	3.90
Sn–I (Å)	3.10	3.22 (Sn <sup>2+</sup> )	2.85	3.04 (Sn <sup>2+</sup> )
		2.89 (Sn <sup>4+</sup> )		2.71 (Sn <sup>4+</sup> )
I–I (Å)	4.39	4.40	4.04	4.04

To further discuss the oxidation state of Sn, we performed Bader charge analysis for Cs<sub>2</sub>SnI<sub>6</sub> as well as other related compounds for comparison (see Table S2 in Supporting Information). The Cs atom in Cs<sub>2</sub>SnI<sub>6</sub> loses  $0.85e^-$  charge and, therefore, almost in the charge state of +1, as the usual case for alkali metals. For Sn, the oxidation states (Z) calculated from the Bader charges (N) are summarized in Figure 5. The Sn in Cs<sub>2</sub>SnI<sub>6</sub> has the Z = +1.24, close to those in CsSnI<sub>3</sub> (+0.89), binary SnI<sub>2</sub> (+0.98), and SnI<sub>4</sub> (+1.16), indicating that the Sn in these compounds have similar oxidation states, close to the formal charge of +2. The similarity in the Z values between Cs<sub>2</sub>SnI<sub>6</sub> and CsSnI<sub>3</sub> would be reasonable because the coordination structures around an Sn ion consist of [SnI<sub>6</sub>] octahedra and are similar to each other. Besides, the Z values of the Sn ions in Cs<sub>2</sub>SnI<sub>6</sub> and CsSnI<sub>3</sub> are much closer to the Sn in typical Sn<sup>2+</sup>-based compounds SnO and SnF<sub>2</sub> (+1.25 and +1.56, respectively) than those in the Sn<sup>4+</sup>-based ones, SnO<sub>2</sub> and SnF<sub>4</sub> (+2.40 and +2.71, respectively), further supporting the oxidation states of +2 for the Sn in Cs<sub>2</sub>SnI<sub>6</sub> and CsSnI<sub>3</sub>. Interestingly, the SnI<sub>4</sub> has the similar Z value to that in SnI<sub>2</sub> and other Sn<sup>2+</sup>-based compounds. It implies that, unlike F, anionic I is much larger than F and other halide ions, forms more covalent bonds, and consequently its oxidation ability is not strong enough to oxidize Sn to the +4 oxidation state; SnI<sub>4</sub> is indeed known to be a covalent molecular compound with more covalent I–I bonds.<sup>34</sup>

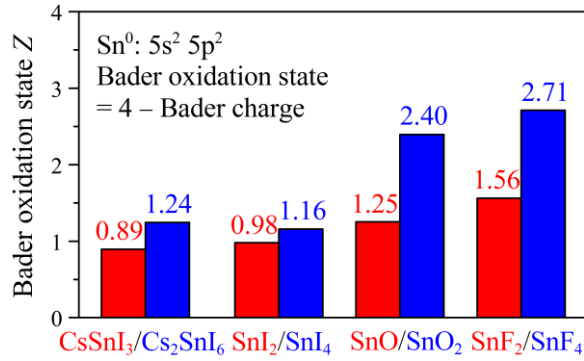


**Figure 5.** Bader oxidation states (Z) of Sn in Sn-based compounds.

**3.6. Origin of Stability.** From the above results, the actual oxidation state is +2, rather than the expected +4. Thus, the expected 4+ oxidation state of Sn cannot explain the improved stability of Cs<sub>2</sub>SnI<sub>6</sub> compared with CsSnI<sub>3</sub>. To examine the stability of Cs<sub>2</sub>SnI<sub>6</sub>, we calculated defect formation enthalpies ( $\Delta H$ ) of Cs, Sn, and I vacancies (V<sub>Cs</sub>, V<sub>Sn</sub>, and V<sub>I</sub>, respectively) for Cs<sub>2</sub>SnI<sub>6</sub> and CsSnI<sub>3</sub> based on defect reaction equations such as Cs<sub>2</sub>SnI<sub>6</sub>  $\Rightarrow$  Cs<sub>2</sub>SnI<sub>6</sub>:V<sub>Cs</sub> + Cs (metal). It shows that all the constituent elements in CsSnI<sub>3</sub> have small  $\Delta H$ , which indicates that the CsSnI<sub>3</sub> phase easily generate these defects and would decompose. For CsSnI<sub>6</sub>, although only  $\Delta H$  of V<sub>I</sub> is small those of V<sub>Cs</sub> and V<sub>Sn</sub>, in particular that of V<sub>Sn</sub>, are much larger than those of CsSnI<sub>3</sub>, explaining the improved stability of the Cs<sub>2</sub>SnI<sub>6</sub> phase. The large  $\Delta H$ , in particular for V<sub>Sn</sub>, in Cs<sub>2</sub>SnI<sub>6</sub> is understood by the shortened bonding distance and consequent stronger covalence of the Sn–I bonds.

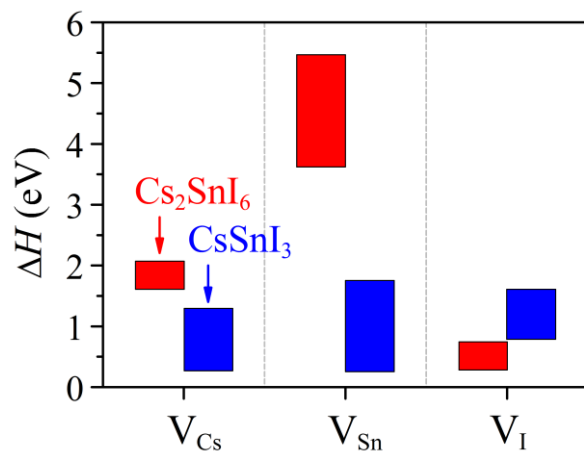


**Figure 6.** Defect formation enthalpies ( $\Delta H$ ) of Cs, Sn, and I vacancies (V<sub>Cs</sub>, V<sub>Sn</sub>, and V<sub>I</sub>) in Cs<sub>2</sub>SnI<sub>6</sub> in comparison with those of CsSnI<sub>3</sub>. The data of CsSnI<sub>3</sub> are taken from Ref. 17.

## 4. CONCLUSIONS

We conclude that the real charge state of Sn in  $\text{Cs}_2\text{SnI}_6$  is +2, which is the same as that in  $\text{CsSnI}_3$  but different from the previously-expected value +4. DFT calculations clarified a strong covalent nature of the Sn–I bonds in the  $[\text{SnI}_6]$  clusters, leading to the formation of  $\text{I} 5\text{p} - \text{Sn} 5\text{s}$  antibonding conduction band and transferring electrons to the Sn ion to stabilize the +2 oxidation state. The present result also explain the improved stability of the  $\text{Cs}_2\text{SnI}_6$  phase. The  $\text{Sn}^{2+}$  state and the apparently  $\text{I}^{-2/3}$  state form the shortened and strengthened Sn–I chemical bonds. The shortened and stronger Sn–I bonds would be a consequence of the crystal structure of  $\text{Cs}_2\text{SnI}_6$  because the isolation of the  $[\text{SnI}_6]$  cluster network allows the  $[\text{SnI}_6]$  clusters more structural flexibility and shortens the Sn–I and I–I bonds, similar to stable functional groups like  $[\text{SO}_4]^{2-}$ .

The present result also shows the conventional ionic model is invalid for p-block metal-iodide based perovskites in which ionic bonds and covalent bonds coexist and compete, and provides a guiding principle to design new perovskite-based photovoltaic materials.

## ASSOCIATED CONTENT

**Supporting Information.** Band energy eigenvalues and occupancy for  $\text{I}_6^0$  and  $[\text{SnI}_6]^{2-}$  models, and the detailed results of the Bader charge analysis are supplied in Supporting Information. This material is available free of charge via the Internet at <http://pubs.acs.org>.

## ACKNOWLEDGMENT

This work was conducted under Tokodai Institute for Element Strategy (TIES) by MEXT Elements Strategy Initiative to Form Core Research Center. We would like to thank Prof. Nitin P. Padture at Brown University for his support and advice for Y.Z.

## REFERENCES

- (1) Best Research-Cell Efficiencies, National Renewable Energy Laboratory, <http://www.nrel.gov/ncpv/>, November 2015.

(2) Kojima, A.; Teshima, K.; Shirai, Y.; Miyasaka, T. Organometal Halide Perovskite as Visible-Light Sensitizers for Photovoltaic Cells. *J. Am. Chem. Soc.* **2009**, *131*, 6050–6051.

(3) Zhou, H.; Chen, Q.; Li, G.; Luo, S.; Song, T.; Duan, H.-S.; Hong, Z.; You, J.; Liu, Y.; Yang, Y. Interface Engineering of Highly Efficient Perovskite Solar Cells. *Science* **2014**, *345*, 542–546.

(4) Jeon, N. J.; Hoh, J. H.; Kim, Y. C.; Yang, K. S.; Ryu, S.; Seok, S. I. Solvent Engineering for High-Performance Inorganic–Organic Hybrid Perovskite Solar Cells. *Nat. Mater.* **2014**, *13*, 897–903.

(5) Im, J.-H.; Jang, I.-H.; Pellet, N.; Grätzel, M.; Park, N.-G. Growth of  $\text{CH}_3\text{NH}_3\text{PbI}_3$  Cuboids with Controlled Size for High-Efficiency Perovskite Solar Cells. *Nat. Nanotech.* **2014**, *9*, 927–932.

(6) Kutes, Y.; Ye, L.; Zhou, Y.; Pang, S.; Huey, B. D.; Padture, N. P. Direct Observation of Ferroelectric Domains in Solution-Processed  $\text{CH}_3\text{NH}_3\text{PbI}_3$  Perovskite Thin Films. *J. Phys. Chem. Lett.* **2014**, *5*, 3335–3339.

(7) Hao, F.; Stoumpos, C. C.; Cao, D. H.; Chang, R. P. H.; Kanatzidis, M. G. Lead-Free Solid-State Organic–Inorganic Halide Perovskite Solar Cells. *Nat. Photon.* **2014**, *8*, 489–494.

(8) Noel, N. K.; Stranks, S. D.; Abate, A.; Wehrenfennig, C.; Guarnera, S.; Haghhighirad; A.-A.; Sadhanala; A.; Eperon, G. E.; Pathak, S. K.; Johnson, M. B.; Petrozza, A.; Herz; L. M.; Snaith, H. J. Lead-Free Organic–Inorganic Tin Halide Perovskites for Photovoltaic Applications. *Energy Environ. Sci.* **2014**, *7*, 3061–3068.

(9) Chung, I.; Lee, B.; He, J.; Chang, R. P. H.; Kanatzidis, M. G. All-Solid-State Dye-Sensitized Solar Cells with High Efficiency. *Nature* **2012**, *485*, 486–489.

(10) Chung, I.; Song, J.-H.; J. Jino; Androulakis, J.; Malliakas, C. D.; Li, H.; Freeman, A. J.; Kenney, J. T.; Kanatzidis, M. G.  $\text{CsSnI}_3$ : Semiconductor or Metal? High Electrical

Conductivity and Strong Near-Infrared Photoluminescence from a Single Material. High Hole Mobility and Phase-Transitions. *J. Am. Chem. Soc.* **2012**, *34*, 8579–8587.

(11) Zhou, Y.; Garces, H. F.; Senturk, B. S.; Ortiz, A. L.; Padture, N. P. Room Temperature “One-Pot” Solution Synthesis of Nanoscale  $\text{CsSnI}_3$  Orthorhombic Perovskite Thin Films and Particles. *Mater. Lett.* **2013**, *110*, 127–129.

(12) Brik, M. G.; Kityk, I. V. Modeling of Lattice Constant and Their Relations with Ionic Radii and Electronegativity of Constituting Ions of  $\text{A}_2\text{XY}_6$  Cubic Crystals (A=K, Cs, Rb, Tl; X=Tetravalent Cation, Y=F, Cl, Br, I). *J. Phys. Chem. Solids* **2011**, *72*, 1256–1260.

(13) Robertson, J. Electronic Structure of  $\text{SnO}_2$ ,  $\text{GeO}_2$ ,  $\text{PbO}_2$ ,  $\text{TeO}_2$  and  $\text{MgF}_2$ . *J. Phys. C: Solid State Phys.* **1979**, *12*, 4767–4776.

(14) Lee, B.; Stoumpos, C. C.; Zhou, N.; Hao, F.; Malliakas, C.; Yeh, C.-Y.; Marks, T. J.; Kanatzidis, M. G.; Chang, R. P. H. Air-Stable Molecular Semiconducting Iodosalts for Solar Cell Applications:  $\text{Cs}_2\text{SnI}_6$  as a Hole Conductor. *J. Am. Chem. Soc.* **2014**, *136*, 15379–15385.

(15) Frost J. M.; Butler K. T.; Brivio F.; Hendon C. H.; van Schilfgaarde M.; Walsh A. Atomistic Origins of High-Performance in Hybrid Halide Perovskite Solar Cells. *Nano Lett.* **2014**, *14*, 2584–2590.

(16) Feng, J.; Xiao, B. Crystal Structures, Optical Properties, and Effective Mass Tensors of  $\text{CH}_3\text{NH}_3\text{PbX}_3$  (X = I and Br) Phases Predicted from HSE06. *J. Phys. Chem. Lett.* **2014**, *5*, 1278–1282.

(17) Xu, P.; Chen, S.; Xiang, H.-J.; Gong, X.-G.; Wei, S.-H. Influence of Defects and Synthesis Conditions on the Photovoltaic Performance of Perovskite Semiconductor  $\text{CsSnI}_3$ . *Chem. Mater.* **2014**, *26*, 6068–6072.

(18) Mulliken, R. S. Electronic Population Analysis on LCAO-MO Molecular Wave Functions. I. *J. Chem. Phys.* **1955**, *23*, 1833–1840.

(19) Bader, R. F. W. *Atoms in Molecules*; Oxford University Press: Oxford, 1994.

(20) Gonze, X.; Lee, C. Dynamical Matrices, Born Effective Charges, Dielectric Permittivity Tensors, and Interatomic Force Constants from Density-Functional Perturbation Theory. *Phys. Rev. B* **1997**, *55*, 10355.

(21) Kresse, G.; Furthmüller, J. Efficient Iterative Schemes for *Ab Initio* Total-Energy Calculations Using a Plane-Wave Basis Set. *Phys. Rev. B* **1996**, *54*, 11169–11186.

(22) Perdew, J. P.; Burke, K.; Ernzerhof, M. Generalized Gradient Approximation Made Simple. *Phys. Rev. Lett.* **1996**, *77*, 3865–3868.

(23) Heyd, J.; Scuseria, G. E.; Ernzerhof, M. Erratum: “Hybrid Functionals Based on a Screened Coulomb Potential” [J. Chem. Phys. 118, 8207 (2003)]. *J. Chem. Phys.* **2006**, *124*, 219906.

(24) Savin, A.; Jepsen, O.; Flad, J.; Andersen, O. K.; Preuss, H.; von Schnering, H. G. Electron Localization in Solid-State Structures of the Elements: the Diamond Structure. *Angew. Chem., Int. Ed. Engl.* **1992**, *31*, 187–188.

(25) Momma K.; Izumi F. VESTA 3 for Three-Dimensional Visualization of Crystal, Volumetric and Morphology Data. *J. Appl. Crystallogr.* **2011**, *44*, 1272–1276.

(26) Dronskowski, R.; Blöchl, P. E. Crystal Orbital Hamilton Populations (COHP): Energy-Resolved Visualization of Chemical Bonding in Solids Based on Density-Functional Calculations. *J. Phys. Chem.* **1993**, *97*, 8617–8624.

(27) Jepsen, O.; Burkhardt, A.; Andersen, O. K. The Program TB-LMTO-ASA, *Version 4.7*; Max-Planck-Institut für Festkörperforschung, Stuttgart, Germany, 1999.

(28) Tang, W.; Sanville, E.; Henkelman, G. A Grid-Based Bader Analysis Algorithm without Lattice Bias. *J. Phys.: Condens. Matter.* **2009**, *21*, 084204.

(29) Werker W. Die Krystallstruktur des  $Rb_2SnJ_6$  und  $Cs_2SnJ_6$ . *Recl. Trav. Chim. Pays-Bas Belg.* **1939**, *58*, 257–258.

(30) Xiao, Z.; Hiramatsu, H.; Ueda, S.; Toda, Y.; Ran, F.-Y.; Guo, J.; Lei, H.; Matsuishi, S.; Hosono, H.; Kamiya, T. Narrow Bandgap in  $\beta$ -BaZn<sub>2</sub>As<sub>2</sub> and Its Chemical Origins. *J. Am. Chem. Soc.* **2014**, *136*, 14959–14965.

(31) Vajenine, G. V.; Hoffmann, R. Magic Electron Counts for Networks of Condensed Clusters: Vertex-Sharing Aluminum Octahedra. *J. Am. Chem. Soc.* **1998**, *120*, 4200–4208.

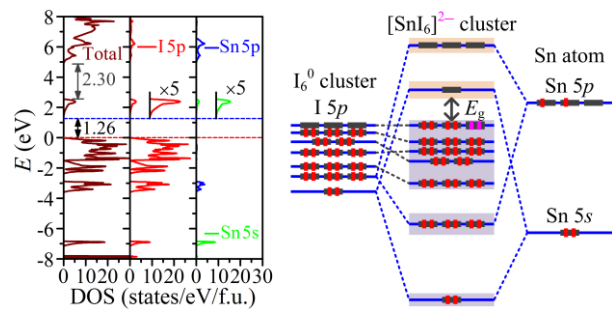
(32) Shannon, R. D. Revised Effective Ionic Radii and Systematic Studies of Interatomic Distances in Halides and Chalcogenides. *Acta Cryst.* **1976**, *A32*, 751–767.

(33) Atkins, P. W.; Overton, T. L.; Rourke, J. P.; Weller, M. T.; Armstrong, F. A. *Inorganic Chemistry*, 5<sup>th</sup> ed.; Oxford University Press: New York, 2010; p 783.

(34) Cordey-Hayes, M. The Mössbauer Effect in Some Organic Tin Halides. *J. Inorg. Nucl. Chem.* **1964**, *26*, 915–923.

(35) Zhang, J.; Yu, C.; Wang, L.; Li, Y.; Ren, Y.; Shum, K. Energy Barrier at the N719-Dye/CsSnI<sub>3</sub> Interface for Photogenerated Holes in Dye-Sensitized Solar Cells. *Sci. Rep.* **2014**, *4*, 6954.

## TOC GRAPHICS



## SUPPORTING INFORMATION

**Table S1.** Energy eigenvalues and occupancies at the  $\Gamma$  point for isolated  $I_6^0$  and  $[SnI_6]^{2-}$  octahedron.

$I_6^0$ octahedron ( $E_F = -6.154$ eV)			$[SnI_6]^{2-}$ octahedron ( $E_F = -4.524$ eV)		
Band Index	Band Energy	Occupancy	Band Index	Band Energy	Occupancy
1	-18.620	2	1	-17.457	2
2	-18.333	2	2	-16.707	2
3	-18.333	2	3	-16.707	2
4	-18.333	2	4	-16.707	2
5	-18.193	2	5	-16.429	2
6	-18.193	2	6	-16.429	2
7	-7.834	2	7	-11.175	2
8	-7.357	2	8	-7.295	2
9	-7.357	2	9	-7.295	2
10	-7.357	2	10	-7.295	2
11	-7.346	2	11	-5.935	2
12	-7.346	2	12	-5.935	2
13	-7.346	2	13	-5.935	2
14	-6.520	2	14	-5.174	2
15	-6.520	2	15	-5.174	2
16	-6.520	2	16	-5.084	2
17	-6.277	2	17	-5.084	2
18	-6.277	2	18	-5.084	2
19	-6.159	2	19	-5.008	2
20	-6.159	2	20	-5.008	2
21	-6.159	2	21	-5.008	2
22	-5.834	0	22	-4.526	2
23	-5.834	0	23	-4.526	2
24	-5.834	0	24	-4.526	2
25	0.251	0	25	-2.169	0
26	1.339	0	26	-0.239	0
27	1.339	0	27	0.927	0
28	1.490	0	28	0.927	0
29	1.490	0	29	0.927	0
30	1.490	0	30	0.948	0
31	1.842	0	31	0.948	0
32	1.966	0	32	1.158	0
33	2.179	0	33	1.739	0
34	2.282	0	34	1.739	0
35	2.282	0	35	1.739	0
36	2.282	0	36	2.047	0
37	2.322	0	37	2.047	0
38	2.322	0	38	2.047	0
39	2.322	0	39	2.107	0
40	2.617	0	40	2.107	0
41	2.617	0	41	2.107	0
42	2.717	0	42	2.384	0
43	2.717	0	43	2.384	0
44	2.717	0	44	2.394	0
45	3.225	0	45	2.394	0
46	3.225	0	46	2.394	0
47	3.225	0	47	2.578	0
48	3.238	0	48	2.673	0

**Table S2.** Bader charges (N), oxidation states (Z), and allocated volume for each ion in Sn-based semiconducting compounds.

Compound		Sn			X (X = O, F and I)			Cs		
Formula	Space group	N	Z	Volume (Å)	N	Z	Volume (Å)	N	Z	Volume (Å)
SnO	<i>P</i> 4/nmm	2.75	+1.25	21.8	7.25	-1.25	12.91			
SnO <sub>2</sub>	<i>P</i> 42/mnm	1.61	+2.40	10.12	7.20	-1.20	12.81			
SnF <sub>2</sub>	<i>C</i> 12/m1	2.44	+1.56	23.34	7.781	-0.78	15.66			
SnF <sub>4</sub>	<i>I</i> 4/mmm	1.29	+2.71	9.50	7.68	-0.68	13.91			
SnI <sub>2</sub>	<i>C</i> 12/m1	3.02	+0.98	26.82	7.49	-0.49	44.77			
SnI <sub>4</sub>	<i>Pa</i> -3	2.84	+1.16	21.90	7.29	-0.29	52.04			
CsSnI <sub>3</sub>	<i>Pm</i> -3m	3.11	+0.89	27.98	7.59	-0.59	54.70	8.13	+0.87	48.93
Cs <sub>2</sub> SnI <sub>6</sub>	<i>Fm</i> -3m	2.76	+1.24	19.23	7.49	-0.49	52.05	8.15	+0.85	42.81